Quantum Interference Control of Electrical Currents in GaAs

A. Haché, J. E. Sipe, and H. M. van Driel

Abstract—In an earlier publication, preliminary observations of the generation of electrical currents were reported in GaAs and low-temperature-grown GaAs (LT-GaAs) at 295 K using quantum interference control of single- and two-photon band–band absorption of 1.55- and 0.775-μm ultrashort optical pulses. Time-integrated currents were measured via charge collection in a metal–semiconductor–metal (MSM) electrode structure. Here we present detailed characteristics of this novel effect in terms of a simple circuit model for the MSM device and show how the injected current depends on MSM parameters as well as optical coherence, power, and polarization. For picosecond pulse excitation with peak irradiance of only 30 MW/cm^{-2} (1.55 μm) and 9 kW/cm^{-2} (0.775 μm), peak current densities of $\sim$10 A/cm^{-2} at peak carrier densities of 10^{15} cm^{-3} are inferred from the steady-state signals. This compares with 50 A/cm^{-2} predicted theoretically; the discrepancy mainly reflects inefficient charge collection at the MSM electrodes.

Index Terms—Interference, photoconductivity, quantum effect semiconductor devices, ultrafast electronics.

I. INTRODUCTION

THE FREQUENCY and intensity properties of lasers have long been used to probe and even alter properties of matter. However, the most characteristic property of laser light, namely its well-defined phase, is rarely regarded as a control parameter. The possibility of so employing laser phase was first proposed by Manykin and Alfanas'ev [1], who considered the interference of quantum mechanical transition amplitudes for two pathways coupling the same initial and final states of an atom. In particular, they suggested that simultaneous single- and three-photon absorption could control state populations and hence the transmission of the medium. This is analogous to the interference of two beams in a Young's double slit experiment, as shown in Fig. 1(a), except that now one has an effective "matter interferometer," since it is electrons that are being controlled. Both passive and active quantum interference control (QUIC), or as it is sometimes called, coherence control, of electron populations have now been considered and demonstrated in atomic and diatomic gases [2]–[7], in impurity atoms assisting second harmonic generation in optical fibers [8]–[10], and in semiconductor
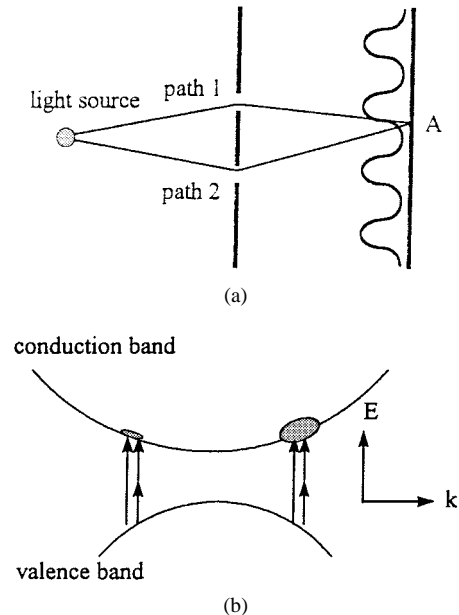
Fig. 1. (a) Interference effects in a Young's double slit experiment. (b) Conceptual diagram of interference between single- and two-photon processes connecting the same valence and conduction bands in a direct bandgap semiconductor leading to asymmetrical distributions of electrons (hole distribution is not shown).

quantum wells (QW's) at 5 K [11], [12]. Branching ratios in elementary photochemical reactions [13]–[16] have also been controlled.

The conventional wisdom is that ultrafast decoherence processes would make QUIC processes difficult to observe in complex systems such as polyatomic molecules and solids. For large molecules, this is still apparently the case, but for solids QUIC mechanisms have been theoretically proposed to generate and induce current flow in semiconductors via multiple-beam free-carrier absorption [17], photoionization of doublet donor states [18], or, more generally, using band–band transitions in bulk semiconductors [19]–[23]. Directional ionization effects have been demonstrated experimentally in various systems using phase- and harmonically related optical beams. Coherently controlled photoemission from Cs–Sb surfaces has been reported by Zel'dovich *et al.* [24], [25], who used 1.06- and 0.53-μm picosecond pulses. Shortly thereafter, Yin *et al.* demonstrated directional ionization of atomic rubidium using nanosecond 564- and 282-nm pulses [26]. Dupont *et al.* [27] observed the solid-state analog of this atomic effect by directionally ionizing electrons from GaAs–AlGaAs QW's at 80 K using 10.6- and 5.3-μm nanosecond pulses. Building

on our theoretical proposal of QUIC photocurrents in a bulk solid [19]–[22], the present authors and co-workers demonstrated [28] QUIC currents in GaAs and low-temperature-grown GaAs (LT–GaAs) using a metal–semiconductor–metal (MSM) device illuminated by 1.55- and 0.775-μm picosecond and femtosecond pulses. One of the reason that QUIC effects can involve continuum states in bulk crystalline media is related to translational symmetry. The restrictive selection rules require conservation of momentum in electron–hole scattering processes, limiting the typical scattering time to values of 100 fs or longer, rather than the much shorter time for amorphous media or even large molecules. Indeed, it is this "high" value of the carrier momentum relaxation time that gives rise to the large mobility observed in, e.g., GaAs and allows conventional current to be generated in crystalline solids under dc-electric field bias. The other reason why QUIC effects may be observed in bulk semiconductors is that all the conduction and valence band states which are coupled by the excitation pulses can contribute to current flow. These two aspects makes QUIC current generation in solids more amenable than other forms of QUIC phenomena, such as photoreactions in large molecules, where the goal is to target a *particular* quantum state and/or break a *particular* bond in the presence of rapid decoherence phenomena.

In this paper, we characterize the QUIC photocurrent effects in GaAs and LT–GaAs at 295 K in a steady-state regime in terms of the MSM device characteristics and the optical pulse polarization, power, and coherence properties. In the following section, we offer the basic phenomenology for our experiments while Section III discusses the experimental apparatus. Section IV gives experimental results for QUIC currents as a function of MSM and beam parameters and, finally, Section V provides some conclusions and possibilities for future work.

II. QUIC PHENOMENOLOGY

We consider QUIC of electron–hole pairs via simultaneous single- and two-photon absorption of coherently related beams of frequency ω and 2ω, for the case where $\hbar\omega < E_g < 2\hbar\omega$ with E_g being the semiconductor bandgap (see Table I for the value of this and other material parameters for GaAs [29], [30])[1]. It was shown [22] that the interference of quantum mechanical pathways leads to an electron and hole (e, h) current *injection* process whose rate $\dot{\boldsymbol{J}}^{\mathrm{I}}_{\mathrm{e,h}}$ is related to the two optical electric fields,[2] $\boldsymbol{E}^{\omega}$, $\boldsymbol{E}^{2\omega}$ by

$$\dot{\boldsymbol{J}}^{\mathrm{I}}_{\mathrm{e,h}} = \overleftrightarrow{\eta}_{\mathrm{e,h}} : \boldsymbol{E}^{\omega}\boldsymbol{E}^{\omega}\boldsymbol{E}^{-2\omega} + \mathrm{c.c.} \qquad (1)$$

where $\overleftrightarrow{\eta}_{\mathrm{e,h}}$ is a fourth-rank purely imaginary tensor, which for a semiconductor with zinc-blend symmetry has four independent components, the largest being $(\overleftrightarrow{\eta}_{\mathrm{e,h}})_{\mathrm{xxxx}}$. (QUIC current injection has also been observed for three phase-related beams with different frequencies, ω_1, ω_2, and $\omega_1 + \omega_2$ with $\hbar\omega_1$, $\hbar\omega_2 < E_g < \hbar(\omega_1 + \omega_2)$; we defer a discussion of this to a future publication [31].) Fig. 1(b) schematically

---

[1]Note: The optical parameters of LT–GaAs and GaAs do not differ significantly for photons with energy >100 meV above the bandgap.

[2]We use the convention that for a monochromatic beam $\mathbf{E}(t) = \mathbf{E}^{\omega}\exp(-i\omega t) + \mathrm{c.c.}$

TABLE I
ELECTRICAL AND OPTICAL PARAMETERS FOR GaAs AND LT-GaAs AT 295 K

Parameter	Value
α (linear absorption coefficient)	1.5×10^4 cm^{-1} (at 775 nm) [29], [30]
β (two-photon absorption coefficient)	5 cm/GW (1.55 μm [32] 25 cm/GW [22]
n (refractive index)	3.70 (775 nm); 3.37 (1.55 μm) [30]
E_g (bandgap energy)	1.43 eV [29]
R (reflectivity)	0.33 (775 nm); 0.29 (1.55 μm) [30]
η_{xxxx} (element of current injection tensor)	20 s^{-2}·mcV^{-3} (775 nm); 0.29 (1.55-μm pulses) [22]
m_e (electron effective mass)	$0.07m_0$ [29]
m_h (heavy hole effective mass)	$0.5m_0$ [29]
μ_e (electron mobility)	8000 cm^2·V^{-1}·s^{-1} (GaAs); 1000 cm^2·V^{-1}·s^{-1} (LT-GaAs) [40], [41]
τ_e (electron momentum relaxation time)	180 fs [38], [340
τ_r (carrier recombination time)	See text.
D_a (ambipolar diffusion coefficient)	20 cm^2·s^{-1} [29]

illustrates the band–band absorption processes that can lead to polar distributions of electrons in momentum (k) space. For the experiments discussed here the optical pulses have center wavelengths of 1.55 μm and 775 nm, respectively, so chosen since 1.55 μm pulses are the foundation of much of communications technology. Unless otherwise stated we therefore identify such pulses as the ω and 2ω pulses.

In (1) it is assumed that the current relaxation time is long compared to the period of the optical beams so that decay effects can be treated separately. We do so phenomenologically by writing a dynamical equation for the evolution of the current density $\boldsymbol{J}_{\mathrm{e,h}}$ as

$$\dot{\boldsymbol{J}}_{\mathrm{e,h}} = \dot{\boldsymbol{J}}^{I}_{\mathrm{e,h}} - \boldsymbol{J}_{\mathrm{e,h}}/\tau_{\mathrm{e,h}} \qquad (2)$$

where $\tau_{\mathrm{e,h}}$ is the current relaxation time. For both beams polarized along the crystalline x axis, the rate of change of current can be expressed explicitly as

$$(\dot{J}_{\mathrm{e,h}})_{\mathrm{x}} = 2|(\eta_{\mathrm{e,h}})_{\mathrm{xxxx}}|E^{\omega}_x E^{\omega}_x E^{-2\omega}_x \sin(2\phi_{\omega} - \phi_{2\omega})$$
$$- (J_{\mathrm{e,h}})_{\mathrm{x}}/\tau_{\mathrm{e,h}} \qquad (3)$$

where ϕ_{ω} and $\phi_{2\omega}$ are the phases of the two optical beams; henceforth we use $\Delta\phi = 2\phi_{\omega} - \phi_{2\omega}$. Equation (3) directly shows how the phase parameter $\Delta\phi$ can be used to control the current direction and magnitude. Because the effective mass of holes is typically much greater than that of electrons, the kinetic energy and speed of holes is much less than that of the electrons; holes therefore make a much smaller contribution to the electrical current than electrons and indeed [22] $|\eta_{\mathrm{h}}| \ll |\eta_{\mathrm{e}}|$. We therefore neglect the hole current in what follows as Fig. 1(b) suggests and drop the e, h subscripts.

The 2ω and ω pulses also give rise to linear and two-photon optical absorption respectively, injecting an electron–hole density N such that

$$\dot{N} = \frac{1}{2\hbar\omega}[\alpha I^{2\omega} + \beta(I^{\omega})^2] - D_a\nabla^2 N - N/\tau_r \qquad (4)$$

where α is the (single-photon) absorption coefficient for 2ω photons and β is the two-photon absorption coefficient at ω (see Table I); $I^{2\omega,\omega}$ are the (depth-dependent) irradiances of the (2ω, ω) beams whose incident irradiances are $I_0^{2\omega,\omega}$; D_a is the amipolar diffusion coefficient and τ_r is the (possibly density-dependent) carrier recombination time. The characteristic depth of carrier generation is the lesser of α^{-1} and $(\beta I_0^\omega)^{-1}$.

Fig. 2 shows how a QUIC current differs from a conventional current that occurs in a semiconductor when *existing* carriers move in response to a dc electric field. In the case of a QUIC current, electrons are *optically injected* into band states consistent with conservation of energy with a speed $[2(2\hbar\omega - E_g)/m_e(1 + m_e/m_h)]^{0.5}$ which in GaAs is 850 km·s^{-1} for a 150-meV excess energy. When electrons are excited by a single pulse (either the ω or the 2ω pulse acting alone), although there may be anisotropic state-filling [33], [34], the electron distribution is *not polar* in momentum space, i.e., there is no electrical current. However, when single- and two-photon absorption processes both couple the same states, their parity-sensitive quantum mechanical transition amplitudes can interfere. This leads to enhanced generation of carriers with certain crystal momentum k and a decreased generation rate of carriers with momentum $-k$. Electron and hole electrical currents are created in a direction governed by the beams' polarization. The *macroscopic* speed of the injected electron (corresponding to the drift speed of the electrons in the conventional current case) is simply given by $v = \dot{J}/e\dot{N}$. This of course will drop due to relaxation effects. From (1)–(4) it is straightforward to show that this macroscopic speed approaches zero as either beam irradiance approaches zero and that the maximum speed is obtained when $\alpha I^{2\omega} = \beta(I^\omega)^2$. The maximum speed is observed when the quantum mechanical amplitudes for generating e–h pairs via single- and two-photon absorption processes are identical and the two "arms" of the matter interferometer are balanced. This corresponds to a situation of maximum fringe visibility in a Young's double slit experiment.

The maximum macrosocopic speed of injected electrons is given by

$$v_{\max} = \frac{\hbar\omega}{\sqrt{2}\varepsilon_0^{3/2}c^{3/2}n_\omega(n_{2\omega})^{1/2}}|(\eta)_{\text{xxxx}}|\frac{1}{(\alpha\beta)^{1/2}} \quad (5)$$

where $n_{\omega,2\omega}$ are the appropriate refractive indices. For $|(\eta)_{\text{xxxx}}| \sim 20$ s^{-2}·mC·V^{-3} and the values of the parameters indicated in the table, $v_{\max}$ is 500 km·s^{-1}, close[1] to the 850 km·s^{-1} speed of each *individual* electron. Assuming $I_0^\omega = 90$ MW/cm^{-2} and $I_0^{2\omega} = 15$ kW/cm^{-2} [satisfying the irradiance condition leading to (5)] with Gaussian pulsewidths $\tau_\omega = \tau_{2\omega} = \tau_e = 100$ fs, one obtains a surprisingly large peak current ~ 1 kA/cm^{-2} for a carrier density of only 10^{14} cm^{-3}.

---

[1] From the *calculated* value of η_{xxxx} and β (this is based on scaling rules as outlined in, e.g., [32]) as given in Table I, the maximum macroscopic speed exceeds that of the individual electrons by 2×. However, if one self-consistently uses the values of η_{xxxx} and β calculated in [22] using the same band-structure, $v_{\max}$ is $\sim 75\%$ of an individual electron's initial speed. For the remainder of the text we base all theoretical current calcuations on the self-consistent approach.
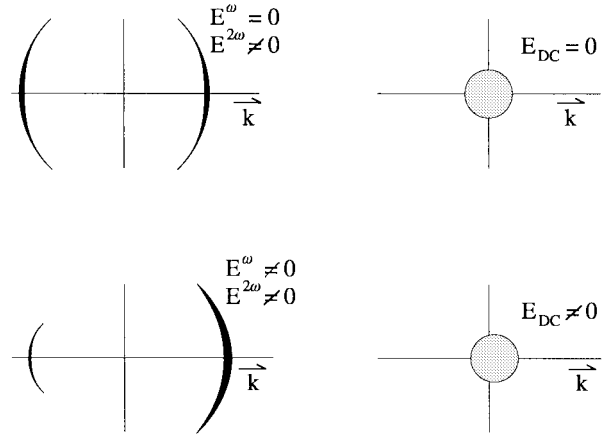

Fig. 2. Schematic of the current distribution in momentum space ($\mathbf{k}$) for QUIC and conventional current generation. The solid curves in the QUIC case indicate (by their density) the selective population of $\mathbf{k}$ states immediately following optical excitation by optical pulses with fields E^ω and $E^{2\omega}$ and the shaded areas in the conventional current case illustrate the population of $\mathbf{k}$ states up to the Fermi level in the presence of a dc electric field.

The current production in the QUIC and conventional cases also differ with respect to their dynamics. For a QUIC current generated via band–band transitions, the carriers obtain their speed in femtoseconds, although of course with the current rise time dictated by the optical pulse rise time. In the case of normal current production, existing carriers are accelerated by an electric field and the momentum distribution is never far from isotropic, as Fig. 2 illustrates. For a carrier density of 10^{15} cm^{-3}, a dc field ~ 8 kV/cm is required to produce $J = 1$ kA·cm^{-2}. In GaAs, with an electron mobility of 8000 cm^2·V^{-1}·s^{-1}, this current would occur ~ 300 fs after the field is "instantaneously" turned on. This illustrates that the QUIC phenomenon more efficiently and quickly produces a large current than can be achieved with the "herding" of statistically distributed electrons.

It should be emphasized that the QUIC currents do not occur as a result of optically generated "dc" electric fields, e.g., through optical rectification acting on preexisting or optically generated carriers. Rectification effects occur via a polarization term of the form $\boldsymbol{P} = \varepsilon_0\chi^{(3)}\boldsymbol{E}^\omega\boldsymbol{E}^\omega\boldsymbol{E}^{-2\omega} + \text{c.c.}$ Such a polarization field is also governed by a fourth-rank tensor which has symmetry and phase characteristics similar to η. Aversa and Sipe [35] have shown that the η tensor is related to a *divergent* piece of $\chi^{(3)}(-\varepsilon; \omega, \omega, -2\omega + \varepsilon)$, i.e., $\eta \propto \varepsilon^2 \lim_{\varepsilon\to 0} \chi^{(3)}(-\varepsilon; \omega, \omega, -2\omega + \varepsilon)$. For GaAs, elements of the nondivergent part of the $\chi^{(3)}$ tensor which leads to the production of a polarization field have a value $<10^{-19}$ m^2/V^{-2} [36], implying that for the irradiances $I_0^\omega = 90$ MW/cm^{-2} and $I_0^{2\omega} = 15$ kW/cm^{-2} a current of <1 mA/cm^{-2} occurs for the optically generated electrons. This is orders of magnitude below the QUIC current value determined by the nondivergent piece of $\chi^{(3)}$. More importantly, the QUIC process is fundamentally different in nature than a field-induced acceleration. This latter process, since it requires separate processes to generate both carriers and the rectification field, will also have a higher power law dependence on the optical beam irradiance. Overall, the QUIC process therefore may offer advantages for physical effects involving

rapid current generation, such as more efficient techniques for terahertz generation.

The $\tau_{e,h}$ time constants strongly influence the peak photocurrent and the rise and fall time of the photocurrent. The current decay time, in addition, may be related to the carrier lifetime since *inter alia*, carrier accumulation or lattice heating can alter dephasing processes. In general, $\tau_{e,h}$ depends on details of the *elastic* and *inelastic* interaction of carriers with phonons, impurities, and defects, and these interactions differ for electrons, heavy holes (hh), and light holes (lh). At 300 K, the e–e scattering rate in GaAs is calculated [37] to range from 0.4 to 60 ps^{-1} for $10^{15} < N < 10^{19}$ cm^{-3} and the e-lh scattering rate varies from 0.05 to 20 ps^{-1} for $10^{17} < N < 10^{19}$ cm^{-3}. The corresponding rates for e-hh interaction are 0.1–2 ps^{-1} for $10^{17} < N < 10^{19}$ cm^{-3}. The rate of bare LO-phonon interactions with electrons is 4.5 ps^{-1} and is independent of density up to 10^{18} cm^{-3}. Experimental measurements [38], [39] of e–e and e-LO-phonon scattering times were found to be in agreement with these calculations. In high-purity GaAs, interactions between carriers of different mass dominate current relaxation for $N > 10^{17}$ cm^{-3}, whereas in the low-density regimes relaxation should be dominated by LO-phonon scattering. In LT–GaAs at 300 K, Prabhu *et al.* [40] measured the electron momentum relaxation rate to be 5.5 ps^{-1} for $N \sim 10^{15}$ cm^{-3}. It is therefore expected that LO-phonon and impurity scattering will dominate the relaxation process in this material for carrier densities up to $\sim 10^{17}$ cm^{-3}.

The principle difference between normal GaAs and LT–GaAs is the carrier trapping or recombination lifetime τ_r. Whereas in GaAs this lifetime is $\gg 1$ ns [29] for $N < 10^{17}$ cm^{-3}, in LT–GaAs the excess arsenic reduces the electron and hole lifetimes to ≤ 1 ps [41], [42]. Hence, although the electrical transport properties of the two material do not differ dramatically, the long carrier lifetime in GaAs can lead to carrier accumulation for long or high repetition rate pulsed excitation. For this reason our initial experiments which focused on the steady-state regime for detecting currents have preferentially employed LT–GaAs. With this material, one can also neglect carrier diffusion effects.

Besides practical considerations to be noted below, there are several fundamental reasons why the theoretical current density might not be attained experimentally. The most important ones are related to phase effects. For example, as the optical pulses enter the semiconductor, linear dispersion can lead to a spatial variation of the optical phase due to a refractive index mismatch for the two beams. As the beams propagate into the semiconductor, the injected current can change direction since the phase parameter $\Delta\phi$ will vary as $\Delta\phi(z) = (2\omega/c)(n_{2\omega} - n_\omega)z$ where z is the depth into the semiconductor. The averaged current injection is therefore given by

$$j^I \propto \int_0^\infty I_\omega(z) I_{2\omega}^{1/2}(z) \sin[\Delta\phi(z) + \Delta\phi_o]\,dz \qquad (6)$$

where $\Delta\phi_o$ is the phase parameter of the beams at $z = 0$. One can show that the ratio between the current injection efficiency for the dispersive versus the ideal case is $\gamma/(\gamma^2 + \delta^2)^{1/2}$ where $\gamma = \beta I_\omega + \frac{1}{2}\alpha$ and $\delta = (2\omega/c)(n_{2\omega} - n_\omega)$. Unless the ω beam
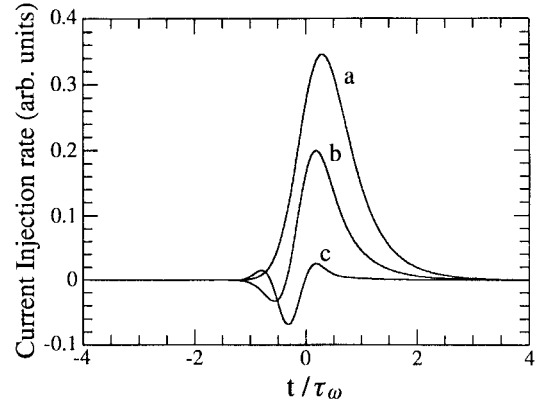

Fig. 3. Theoretical evolution of the current density induced by *chirped* ω and 2ω pulses for delay: (a) 0, (b) 0.5 τ_ω, and (c) τ_ω for both pulses of equal width τ_ω. The current relaxation time is taken to be $\tau_\omega/2$ while the pulse time–bandwidth product = 0.66 for a linearly chirped pulse; $2\omega_o t_d + 2b_\omega t_d^2$ has been set to $\pi/2$.

were to have an irradiance >100 GW/cm^2 γ is determined by the value of α and the peak current is reduced from its ideal value by a factor of ~ 4.

Another important phase effect is related to the use of nontransform-limited pulses. For example, let us consider the effect of a linear frequency chirp in the pulse. Such a chirp can be expressed as [43] $\omega(t) = \omega_o + 2b_\omega t$ with ω_o the center frequency and b_ω the chirp parameter. If the 2ω pulse is derived from such a pulse with a Gaussian envelope profile, there will be a time-varying phase difference between the ω and 2ω pulses as a function of delay, t_d. From Appendix A, we find that (3) is modified so that

$$j_x(b_\omega, t_d) = 2^{5/2} \eta_{\text{xxxx}} (\mu_o/\varepsilon_o)^{3/4} n_\omega n_{2\omega}^{1/2} I_\omega(t) I_{2\omega}^{1/2}(t - t_d)$$
$$\cdot \sin(\Delta\phi(t)) - \frac{J_x}{\tau_e}. \qquad (7)$$

Fig. 3 shows the time dependence of the current density as a function of time delay for moderately chirped pulses $(\tau_\omega \Delta\omega/2\pi = 0.66)$ where $\Delta\omega$ is the bandwidth of the ω pulse. The curves do not peak at zero delay because of the nonzero relaxation time. As the delay increases, the current oscillates and approaches zero. Indeed, as shown in Fig. 4, the integrated current for chirped and delayed pulses drops considerably faster than for transform-limited pulses.

III. EXPERIMENTAL DETAILS

Experiments to observe QUIC currents were carried out using the basic experimental configuration described in [28] and illustrated schematically in Fig. 5(a). Two different optical sources of ω pulses were used. One is an 82-MHz 1-ps-pulse optical parametric oscillator (OPO) [44] with average power, $P^\omega = 100$ mW and pumped by a Kerr-lens mode-locked Ti : sapphire laser. The system is tunable from 1.4 to 1.6 μm and is similar to a femtosecond unit described elsewhere [45]. The output pulses have a time bandwidth product of 0.48, close to the bandwidth limit. The other source is an optical parametric amplifier (OPA) producing pulses with $\sim$150 fs full-width- half-maximum (FWHM) at 250 kHz, with $P^\omega \sim$ 50 mW in the 1.1–1.8-μm range; the time–bandwidth product

(a)   (b)   (c)
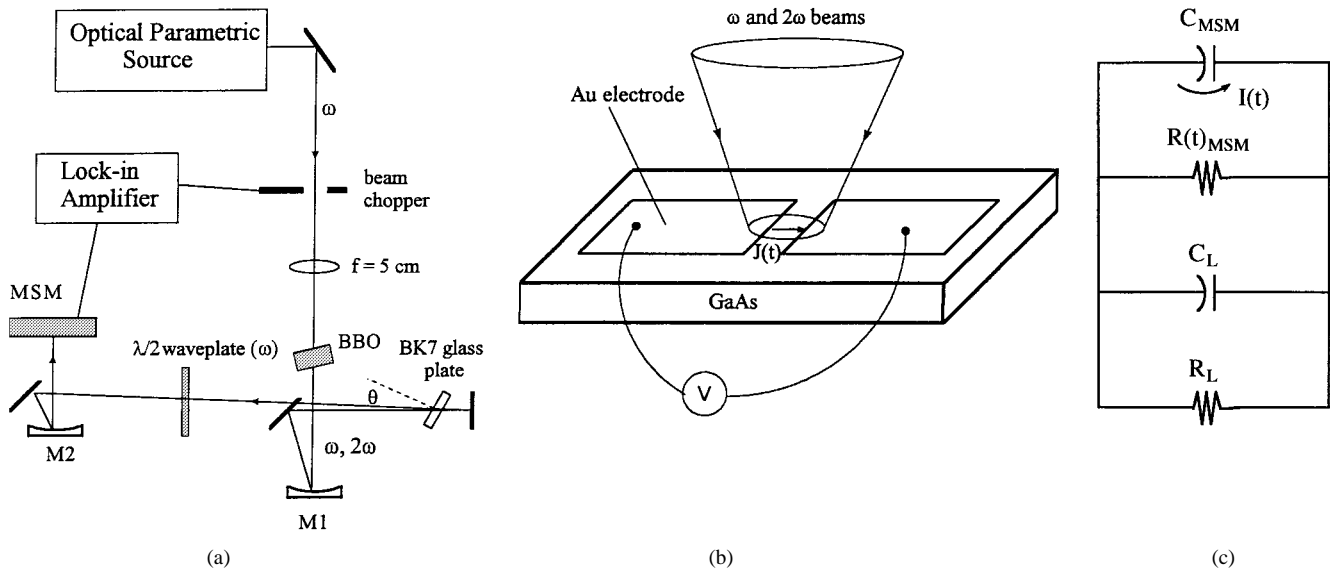
Fig. 5. (a) Diagram of the experimental setup for the coherent control of photocurrent using a parametric source; M1 and M2 are curved mirrors with focal lengths of 10 and 2.5 cm, respectively. (b) Schematic diagram of the illumination geometry and the MSM charge collection device used to monitor a steady-state voltage V. (c) Equivalent circuit diagram of the MSM device and load (voltmeter). Both capacitances (C_{MSM} and C_L) and the load resistance R_L are assumed to remain constant, while the resistance of the MSM gap $R(t)_{\mathrm{MSM}}$ varies due to carrier injection.
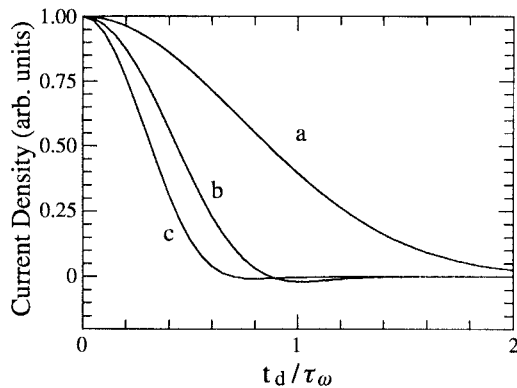

Fig. 4. Calculated integrated current density as a function of time delay for time–bandwidth products of (a) 0.44, (b) 0.66, and (c) 0.88. The current relaxation time is as in Fig. 3.

of the pulses is ∼0.75–0.9, twice the bandwidth limited value; this is not unusual for OPA systems. Phase-related 2ω pulses (near 0.8 μm) are produced in an angle-tuned, 0.6-mm-thick Beta barium borate (BBO) crystal; for both systems the average power $P^{2\omega}$ is <2 mW. The relative phase between the ω and 2ω pulses is varied by passing both through a 1-mm-thick BK7 glass plate for various angles of incidence θ and taking advantage of the different optical path lengths because of the frequency-dependent refractive index. Double passing is used to avoid lateral walkoff between the pulses. The phase parameter $\Delta\phi$ varies with θ according to

$$\Delta\phi = \frac{4\omega\ell_p}{c}\left[\frac{n_{p,\omega}}{\cos\theta_\omega} - \frac{n_{p,2\omega}}{\cos\theta_{2\omega}} - \sin(\tan\theta_\omega - \tan\theta_{2\omega})\right] \tag{8}$$

where $n_{p,\omega} = 1.5013$ and $n_{p,2\omega} = 1.5118$ are the appropriate refractive indices[2] of the glass plate which has thickness $\ell_p =$

[2] Schott Optical Glass, Schott Manufacturing, Duryea, PA USA.

1 mm. The internal angle of propagation of the beams $\theta_{\omega,2\omega}$ is related to θ by $\sin\theta_{\omega,2\omega} = \sin\theta/n_{p,\omega,2\omega}$. The relative polarization of the exiting pulses is controlled using a birefringent plate which acts like a $\lambda/2$ plate for the ω beam but (nearly) a full-wave plate for the 2ω beam. Both pulses are then incident on the gap area of a metal–semiconductor–metal (MSM) structure, as indicated in Fig. 5(b), and the steady-state signal voltage V associated with charge accumulation through current generation is monitored. Although future work will concentrate on detecting time-resolved current, the present configuration allows several effects to be demonstrated in a simple configuration. The present scheme, which effectively monitors the charging of a capacitor, is also much easier to use than an earlier technique wherein charges were collected in quantum wells of different widths, giving rise to luminescence at different wavelengths [19]–[21]. For the MSM device one can relate the steady-state voltage, V, to the peak current density using a simple model of the circuit as indicated in Fig. 5(c). The MSM is assigned a capacitance and a (time-varying) resistance and the external circuit (lock-in amplifier) is modeled as a capacitor in parallel with a resistor. Appendix B provides the details of the relation between V and the peak QUIC current density. Both compensated (resistivity ∼10^8 $\Omega \cdot$ cm) normally grown GaAs and annealed LT–GaAs (resistivity ∼10^7 $\Omega \cdot$ cm) [28] were used in the experiments. The LT–GaAs samples were used for most of the experiments reported here since its rapid carrier trapping time inhibits carrier accumulation effects as noted above. This significantly reduces internal discharge of the MSM device between current injection pulses. Gold electrodes of 170-nm thickness were deposited to produce MSM gaps between 5 and 50 μm; the gaps were oriented along the crystal (100) direction to optimize current injection according to (3). No attempt to produce ohmic contacts using ion-implantation or other techniques were used since these tend to alter sample characteristics significantly in the vicinity of the electrodes.
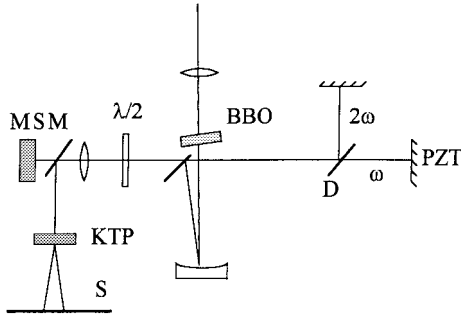
Fig. 6. Apparatus used to control the relative phase of ω and 2ω beams, the latter generated in the BBO crystal. The $\lambda/2$ plate is designed for the 1.55-μm beam and behaves as a full-wave plate for the 0.775-μm beam; the lens has a focal length of 3.8 mm. The right-hand side shows a simple Michelson interferometer used to control the relative phases of beams via a PZ stage before they are incident on an MSM device. When a beam splitter is inserted before the MSM as indicated, the beam profile of the 2ω beam generated from incident ω and 2ω beams in the KTP crystals can be used to monitor beam phase quality.

For many of the experiments, and certainly all those involving the OPA source, a second method for phase control was utilized, based on a Michelson interferometer as shown in Fig. 6. A dichroic mirror (D) splits the beams and a piezoelectric transducer (PZT) is used to control the phase of the beams by adjusting the length of one arm. This technique allows for background-free measurements of QUIC current with rapid phase scan. Lock-in amplification and measurement is made by modulating the phase with the PZT. A square wave voltage is applied to the piezo controller using a function generator to give a displacement amplitude of $\lambda/4$ (or a total of $\lambda/2$ path change for the 1.55-μm beam). Such a displacement makes the phase $\Delta\phi$ vary by half a cycle and allows the signal extrema to be measured in a single sweep. A modulation frequency of 85 Hz was found to be optimum for this purpose. Although the PZT displacement may not be perfectly linear at 85 Hz, the signal periodicity is preserved. Another advantage of using an interferometer for controlling the phase is that the time delay between the pulses can be adjusted, eliminating the need for reflective optics, which were used to prevent pulse temporal walk-off caused by group velocity dispersion in lenses.

Since the current injected into the semiconductor depends on $\Delta\phi$, it is important to preserve the beam phase front quality. The experimental configuration of Fig. 6 includes an apparatus to monitor the phase front quality. If phase matching is satisfied, the value of $\Delta\phi$ inside and at the exit of the BBO crystal is $\pi/2$ across the whole beam. The phase is fixed because the second harmonic beam is initiated in a doubling crystal with zero intensity and its phase is determined by the initial phase of the ω beam. Therefore, phase distortions in a spatially nonideal ω beam are not of great concern. However, after the beam interacts with various optical elements, the phase front could experience some distortion. High-flatness optics ($\lambda/5$ surface flatness or better) are generally used in our coherent control experiments to prevent this. Cascaded frequency doubling constitutes a good diagnostic tool to determine the relative phase of the beams. It consists of generating second harmonic light in one

crystal (BBO in our case) and then mixing the ω and 2ω beams in a KTP (potassium titanyl phosphate) crystal. This technique was used by Chudinov *et al.* [46] to measure the relative phase of two harmonically related beams. The overall conversion efficiency of the ω into 2ω beams depends on the value of $\Delta\phi$ when the waves enter the second crystal. Hence, any relative phase nonuniformity will become apparent in the spatial pattern of the far field of the 2ω beam. For instance, if $\Delta\phi = -\pi/2$, second harmonic light is converted back into the fundamental beam, whereas for $\Delta\phi = \pi/2$ conversion is increased.

IV. RESULTS AND DISCUSSION

QUIC currents have been observed in both LT–GaAs and GaAs. However, although the MSM detectors based on LT–GaAs could be used with either the high repetition rate OPO or lower repetition rate OPA, the GaAs MSM structures only gave evidence for coherence control effects with the OPA. A simple argument illustrates why the lower repetition rate system with approximately the same average power as the OPO is more effective for GaAs in which the carrier lifetime is dominated by bimolecular recombination [29]. Since the 2ω beam is derived from the ω beam by second harmonic generation, as (1) indicates the current or charge injection rate per pulse varies as $(I^\omega)^2$ or $T^2(P^{2\omega})$ where T is the repetition time. However, per pulse, the ability of an MSM gap to contribute to discharge is related to the product of the gap conductivity and carrier recombination time. Since the conductivity is proportional to N and the dominant radiative recombination time varies as N^{-1}, the discharge is effectively independent of peak irradiance or repetition rate. The generation process will therefore dominate internal discharge as the repetition rate drops. Nonetheless, even for the 250-kHz system, which produces peak carrier densities of 10^{18} cm^{-3}, the recombination time is still near 1 μs and the charge integration process is not very effective as the noise in [28, Fig. 3] indicates. We therefore concentrate here on measurements taken with LT–GaAs. Our purpose is to show how QUIC current experiments using the MSM structure can be understood in terms of the simple circuit model, and to illustrate the dependence of the steady-state voltage V on beam polarization, power, and phase-parameter $\Delta\phi$. Additional detailed studies can be found elsewhere [47].

Fig. 7 shows raw data for the dependence of V on θ for MSM's with different electrode gap d. Pulses from the OPO source were used with $I_0^\omega = 5$ MW/cm^{-2} and $I_0^{2\omega} = 9$ kW/cm^{-2} in the configuration of Fig. 3(a) with an ~100-μm spot size. Variations in signal and background amplitudes and modulation depth (as high as 50%) reflect details of the particular MSM and the exact positioning of the beam relative to the MSM gap. The background level is perhaps related to the injection of optically generated carriers by the space-charge field in the vicinity of the contacts. Under optimum conditions we have recorded a modulation amplitude as large as 200 μV (see [28, Fig. 2]) for $I_0^\omega = 30$ MW/cm^{-2} and $I_0^{2\omega} = 9$ kW/cm^{-2}. Using the circuit model, we infer a peak current injection of 10 A/cm^{-2} as compared to a theoretical
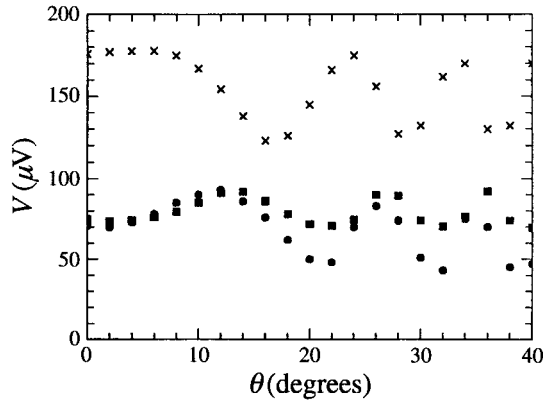
Fig. 7. QUIC current signals as a function of θ from MSM detectors with various pairs of electrodes on a LT–GaAs sample; MSM gap sizes are 5 μm (crosses), 25 μm (circles), and 50 μm (squares).

Fig. 8. Coherent control signal from a 25-μm MSM detector with LT–GaAs for polarizations across (dots) and parallel (squares) to the gap for illumination conditions similar to Fig. 5. A common background signal has been subtracted in each case.

prediction [including correction for effects related to (6)] of 50 A/cm^{-2}. Besides uncertainties in the theoretical values of η and β, the major source of the discrepancy is the poor collection efficiency of surface-mounted electrodes when currents are injected over a depth of nearly a micrometer and into nonohmic contacts. The nonsinusoidal variation of the modulated component of each signal in Fig. 7 is expected, since $\Delta\phi$ is not directly proportional to θ. The figure also illustrates how the experiments are not sensitive simply to a phase difference between beams but to a global phase difference $\Delta\phi$. In particular, the initial phase of the curves [70°, −11°, and −45° for the 5-, 25-, and 50-μm gap samples, respectively, when the raw data are considered in terms of (3)] are different for each gap size. This is due to the fact that the signal amplitude reflects the value of $\Delta\phi$ at the electrode edges since only carriers within a mean free path ($\sim$100 nm) of the electrodes contribute to electrode charging. The value of $\Delta\phi$ cannot be controlled precisely as each MSM device is positioned.

Orientation of the MSM gap along the LT–GaAs (001) direction makes QUIC current generation polarization-sensitive. Fig. 8 shows the QUIC current $\Delta\phi$ dependence of V from a 25-μm gap MSM detector for ω and 2ω beams from the OPO polarized across and parallel to the gap. For data taken with beam polarizations across the gap, a sinusoidal curve gives a good fit to the data and has the appropriate periodicity expected for $\Delta\phi$ values deduced from θ and (8). The data clearly reveal no modulated signal for light fields polarized along the gap consistent with $\eta_{xyy} = 0$ [22]. This also directly illustrates that other possible sources of a phase-varying injected current such as nonlinear/cascaded optical carrier generation in a space-charge field are negligible. Other tests of polarization effects reveal that approximately an order of magnitude weaker signals than the "across gap" case are observed if one of the beams has its polarization along the gap and the other's is across the gap; this is consistent with the relative magnitudes of the η_{xxxx}, η_{xyy}, η_{xxyy} tensor elements [22]. In what follows, all data is obtained with both beams polarized across the MSM gap, taking advantage of the large η_{xxxx} tensor element.

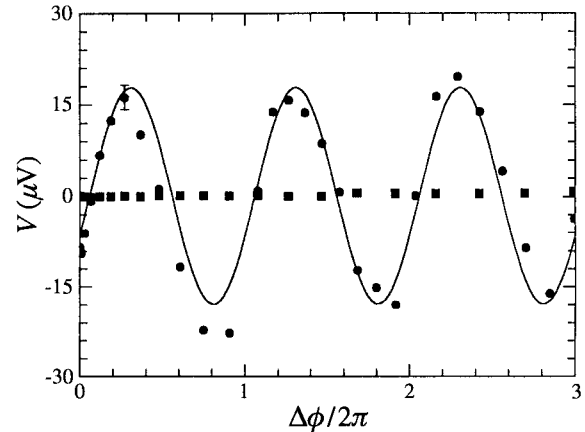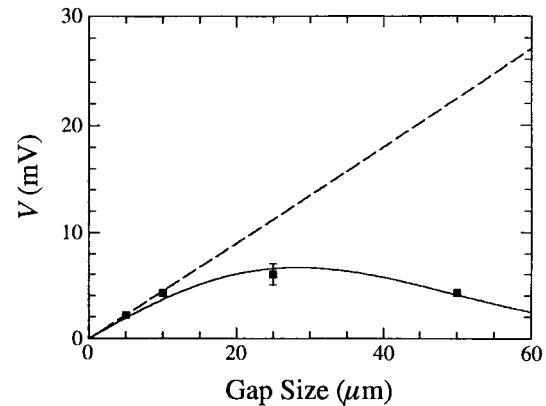Fig. 9 shows how the voltage V varies for MSM devices

Fig. 9. QUIC current signal amplitude from MSM devices with various electrode spacings but under identical conditions of illumination using the OPA source. The dashed line is the response expected for uniform irradiance of the gap while the solid curve is that obtained with Gaussian beam illumination, as discussed in the text.

with four different gap spacings but under identical illumination conditions ($P^\omega \sim 4.5$ mW, $P^{2\omega} \sim 375$ μW) using the OPA optical source. The voltage V is expected to vary with the irradiance at the electrodes and with gap size, since the voltage is proportional to the charge separation. For Gaussian beam profiles, with the beam centered at the middle of the gap, the average voltage should vary with the gap size d according to

$$\langle V(d) \rangle \sim d \exp\left(-4\ln 2\frac{d^2}{s^2}\right) \qquad (9)$$

where s is the spot diameter of the 1.55-μm beam, assumed to be approximately $\sqrt{2}$ larger than that of the 0.775-μm beam. The solid curve, in reasonable agreement with the four data points, is obtained with a beam spot diameter of 70 μm, close to the measured value of 80 μm.

We now consider the scaling of V with the average power P^ω of the fundamental beam. With all other parameters of the beams remaining the same, the conversion of the ω beam into the 2ω beam varies as $(P^\omega)^2$, neglecting pump depletion effects. From (1) one then expects a $(P^\omega)^2$ dependence for
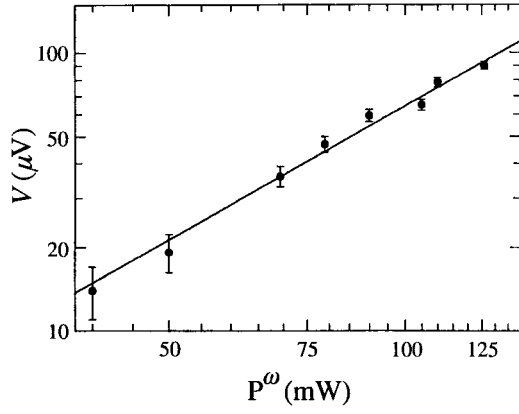
Fig. 10. Steady-state voltage modulation amplitude on a 25-μm gap MSM versus OPO fundamental beam average power P^ω.
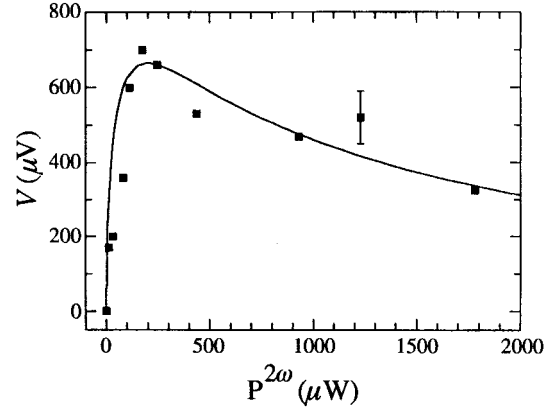

Fig. 11. Signal amplitude from a 10-μm gap LT–GaAs MSM device versus $P^{2\omega}$; the OPA fundamental beam power is maintained at a constant level of 9.5 mW. The solid curve is obtained from the current integration model of the circuit after scaling.

$\dot{J}$. Fig. 10, however, indicates that the signal amplitude varies as $(P^\omega)^{1.6\pm0.2}$ for a 25-μm gap MSM illuminated by pulses from the OPO. The signal, however, is a steady-state voltage V obtained from integrating over not only the temporal profile of each pulse but also many pulses. The space-charge field also involves additional effects such as carrier recombination and displacement in an electric field. With increasing conductivity of the sample, the MSM is also capable of discharging faster, making the MSM a less efficient integrator. Nonetheless, a detailed model for the circuit neglecting space charge effects as outlined in Appendix B gives a power law dependence close to $(P^\omega)^2$. It may be that various density-dependent effects such as carrier screening cause a deviation from quadratic behavior. Clearly, however, the dependence is not cubic or quartic as might occur for rectification fields driving optically generated carriers as outlined in Section II.

The variation of the modulation signal amplitude is also considered as a function of $P^{2\omega}$, with P^ω constant, and is shown in Fig. 11. The $P^{2\omega}$ variation was achieved by small misorientation of the BBO crystal depicted in Fig. 6. The OPA source was used with the beams focused to $\sim$200-μm spot size on an MSM gap with (constant) $I_0^\omega = 10$ GW/cm^{-2}($P^\omega = 9.5$ mW) for the 1.55-μm beam and irradiance $I_0^{2\omega}$ up to 2 GW/cm^{-2}($P^{2\omega} = 1.8$ mW) for the 775-nm beam. The fast rise and slower fall of the curve as $P^{2\omega}$ increases agrees qualitatively with the simple circuit model, represented by the solid curve. (As noted earlier, theoretical estimates of the current exceed that measured. Therefore, the theoretical curve depicted has been scaled to match the peak experimental amplitude.) One can understand the current integration mechanism in terms of two competing processes. In the low power regime the increase reflects $J^I \sim (P^{2\omega})^{0.5}$. However, since the material conductivity increases according to $N \sim I^{2\omega}$ at high power levels, the MSM device resistance is lowered allowing more internal discharge to take place. As a result, there is an optimal level of irradiance beyond which internal discharge dominates and the current integration efficiency decreases. It is clear that the circuit model correctly gives the functional dependence observed in Fig. 11.

With $I_0^\omega = 10$ GW/cm^{-2} and $I_0^{2\omega} = 200$ MW/cm^{-2}, the maximum signal amplitude is 700 μV and the average

current drawn by the lock-in amplifier is 7 pA. Even if discharge took place only through the external circuit, the most conservative estimate of the peak current density is 500 A/cm^{-2} for $N = 7\times10^{17}$ cm^{-3}. If internal dissipation through the MSM is taken into account, the peak current is $>$10 kA/cm^{-2}. This should be compared with a theoretical value of 200 kA/cm^{-2} based on the theoretical value of η_{xxxx} [22] and the model for current integration. Although this may seem large, the current burst only lasts for the $\sim$130-fs pulse duration. It should be noted that time-dependent space-charge effects may significantly reduce charge collection at the carrier densities developed by the OPA pulses, explaining the apparently larger discrepancy between theory and experiment than for the currents generated by OPO pulses.

We now consider how deviations from transform-limited pulses are reflected in the QUIC current characteristics. To do so we consider a linear frequency chirp in the ω pulse, as discussed in Section II. Demonstration of the influence of chirp on the current integration was carried out using the OPA system. Chirped pulses at 1.53 and 0.765 μm were generated using the OPA with an average power of about 5 mW and 500 μW, respectively. First, the pulses' duration were determined by measuring their cross-correlation trace via sum-frequency generation in the KTP crystal since sum-frequency generation is not sensitive to the relative phase of the input pulses or their chirp. The correlation function of two Gaussian pulses is given by

$$e^{-at^2} \otimes e^{-b(t-t_d)^2} \rightarrow e^{[ab/(a+b)]t_d^2} \qquad (10)$$

where a and b are related to the pulse durations and $\otimes$ is the correlation symbol. Consequently, $\tau_{cc}^2 = \tau_\omega^2 + \tau_{2\omega}^2$ where τ_{cc} is the FWHM of the cross-correlation trace. Fig. 12 shows a cross-correlation FWHM of 140 fs, giving values of $\tau_\omega = 115$ fs and $\tau_{2\omega} = 90$ fs assuming the pulses are related by $\tau_{2\omega} = \tau_\omega/\sqrt{2}$ when they leave the doubling crystal. Calculation of $\tau_{2\omega}$ takes into account a spectral bandwidth of 16 nm producing 11 fs of pulse broadening through the quartz waveplate and the 3.8-mm-thick focusing lens shown in Fig. 6. Pulse broadening for the ω beam (bandwidth = 32 nm) is negligible due to the low dispersion of glass and quartz
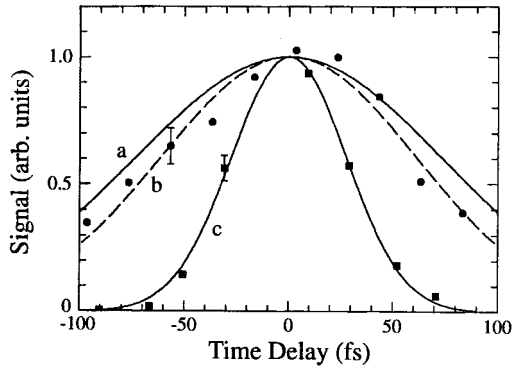
Fig. 12. QUIC current signal and cross correlation versus time delay between 1.53- and 0.765-μm pulses for: (a) expected QUIC current signal with bandwidth-limited pulses, (b) cross-correlation signal via sum frequency generation, and (c) experimentally measured QUIC signal. The FWHM's for each curve are 170, 140, and 65 fs, respectively.
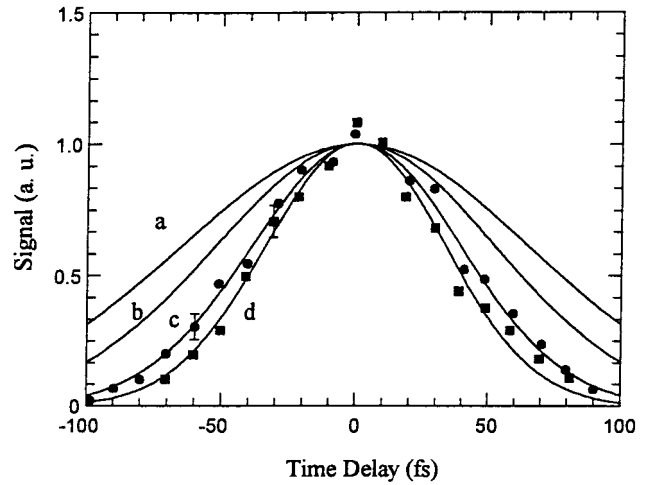

Fig. 13. Gaussian functions representing the measured cross-correlation traces between 1.53- and 0.765-μm pulses (a) after and (b) before chirping of the 0.765-μm pulses and the corresponding coherent control signal amplitude as a function of time delay [curve c (dots) and d (squares)].

at 1.53 μm. From the values of τ_ω and $\tau_{2\omega}$, the width of the coherent control signal amplitude is expected to be $\sim$170 fs, assuming bandwidth-limited pulses (curve a); however, this value is about three times larger than the measured width of 65 fs (curve c). This result is consistent with a time–bandwidth product of about 0.9, according to calculations related to (7) and Fig. 4. Such a large time–bandwidth product is not inconsistent with the characteristics of the OPA.

Fig. 13 shows the result of stretching/chirping one of the optical pulses on the QUIC current. Pulses with width of $\tau_\omega =$ 97 fs and $\tau_{2\omega} = 80$ fs were first used and their cross-correlation trace with width of 125 fs is shown as curve b of Fig. 13. The corresponding coherent control signal curve width is 95 fs (curve c). When a 9.5-mm-thick KZF-2 (Schott glass) flat window was inserted in the path of the 2ω beam (in one arm of the interferometer), the width of the cross-correlation trace increased to 155 fs (curve a) suggesting a new pulse duration of $\tau_{2\omega} = 120$ fs. As a result of the increased chirp, the width of the coherent control signal amplitude was reduced to 80 fs (curve d). If one ignored pulse chirping, a larger width would be evident since one of the pulses is now much longer. In contrast, a reduction by 15 fs is observed. These experiments clearly show the negative impact of the combination of chirp and time delay on the current-integration efficiency, as Fig. 3 also showed.

V. CONCLUSIONS

We have characterized the QUIC currents in LT–GaAs using current collection MSM devices and a simple circuit model. We have also shown the dependence of these currents on semiconductor electrode characteristics and pulse intensity, polarization, and coherence properties. Our results are in good agreement with the circuit model and the theoretical predictions of the coherence and polarization properties expected from the optically generated current. For picosecond pulse peak irradiances of only 30 MW/cm^{-2} (1.55 μm) and 9 kW/cm^{-2} (775 nm), peak current densities of $\sim$10 A/cm^{-2} at peak carrier densities of 10^{15} cm^{-3} are inferred from the steady-state signals as compared to $\sim$50 A/cm^{-2} predicted theoretically; the discrepancy most likely reflects poor charge

collection in our nonohmic electrodes/semiconductor structures. In future we will concentrate on time-resolving the optically generated current and also attempt to observe similar effects in indirect bandgap materials such as silicon.

In principle, the quantum interference scheme offers interesting opportunities for generating and controlling electrical currents in semiconductors. Because the current can be turned on in times dictated by the pulse rise time one can inject high-density currents rapidly, avoiding capacitance and inductance effects associated with controlling currents in conventional circuits. Since the current is controlled only by optical beams, one can also imagine applications in which the temporal and spatial characteristics of the optical pulses can be used as a template to induce currents with similar characteristics in semiconductors. These advantages have been achieved by using nonlinear optical mixing processes which are normally associated with poor conversion efficiency. However, since it is envisioned that one would use the techniques discussed here to generate currents on, e.g., picosecond time scales in information technologies, the irradiances of the pulses used to inject currents would naturally be sufficiently high that the normal limitations of conversion efficiency would be somewhat mitigated.

APPENDIX A
INFLUENCE OF PULSE CHIRP ON CURRENT GENERATION

This appendix provides the basic formalism to describe the effect of pulse chirp on coherently controlled currents. We consider an ω pulse with a linear chirp given by

$$\omega(t) = \omega_o + 2b_\omega t \qquad (A1)$$

with ω_o the center frequency and b_ω the chirp parameter. The relationship of b_ω to the pulse duration τ_ω and frequency bandwidth $\Delta\omega$ in the case of a Gaussian pulse is given by

$$b_\omega = \frac{2\ln 2}{\tau_\omega^2}\left[\left(\frac{\tau_\omega\Delta\omega}{4\ln 2}\right)^2 - 1\right]^{1/2}. \qquad (A2)$$

Hence, if b_ω and $b_{2\omega}$ are the chirp parameters for the ω and 2ω pulses and the pulses are delayed relative to each other by a time t_d, the phase parameter $\Delta\phi$ as a function of time is

$$\Delta\phi(t) = 2\phi_\omega(t + t_d) - \phi_{2\omega}(t) = 2b_\omega(t + t_d)^2 - b_{2\omega}t^2 + 2\omega_o t_d. \tag{A3}$$

When pulse-broadening effects are small in harmonic generation, one can assume that $b_{2\omega} \approx 2b_\omega$ since the ω and 2ω pulses are phase-related. In this case,

$$\Delta\phi(t) = 2b_\omega(2t_d t + t_d^2) + 2\omega_o t_d. \tag{A4}$$

Therefore, a general criterion for chirping to be an important factor in the current injection rate is that

$$4b_\omega t_d \tau_\omega > \pi. \tag{A5}$$

This corresponds to a phase variation greater than 1 rad within a pulse duration. Note that $\Delta\phi$ remains constant if $t_d = 0$. The rate equation for the current generation (3) can be then written

$$\dot{J}_x(b_\omega, t_d) = 2^{5/2}\eta(\mu_o/\varepsilon_o)^{3/4} n_\omega n_{2\omega}^{1/2} I_\omega(t) I_{2\omega}^{1/2}(t - t_d) \cdot \sin(\Delta\phi(t)) - \frac{J_x}{\tau_e} \tag{A6}$$

where η is the appropriate current injection tensor element. Any delay between the pulses will reduce the current injection rate because of smaller pulse envelope overlap and reduce the integrated current because of variation in $\Delta\phi$.

APPENDIX B
CIRCUIT MODEL FOR CURRENT INTEGRATION

The equivalent circuit diagram for the MSM device is illustrated in Fig. 5(c). A voltmeter (commercial lock-in amplifier) is used in parallel with the MSM device, and has a characteristic resistance $R_L = 100$ MΩ and a capacitance $C_L = 25$ pF, for an RC time constant of 2.5 ms. If all the generated QUIC current I were dissipated through the load resistance R_L, one could directly extract the time-averaged current $\langle I \rangle = \langle V(t)/R_l \rangle = V/R_l$ and the peak current $\sim \langle I \rangle \cdot T/\tau_\omega$ where T is the pulse period. However, high carrier densities after illumination of the semiconductor reduce the gap resistance significantly producing internal discharge so that only a small fraction of the current flows through the external circuit. In this model, current integration is described in terms of a charge q accumulated on a capacitor comprised of the MSM and voltmeter. The MSM capacitance C_{MSM} and load capacitance C_l in parallel provide a total capacitance C. The resistors $R_{\mathrm{MSM}}(t)$ and R_l in parallel provide two discharge channels for the current and a total resistance $R(t)$. We consider a source of current $I(t)$ charging the capacitors during illumination with a periodicity such that $I(t) = I(t + T)$. Between and during pulse excitation, discharge occurs with a time constant given by $R(t)C$; the rate equation for q is therefore

$$\dot{q} = -q/R(t)C + I(t). \tag{B1}$$

From (3) the current $I(t)$ satisfies $\dot{I}(t) = \dot{J}(t)S$ where S is the current cross-sectional area (taken as the product of the beam width at the electrode and the optical absorption depth α^{-1}. The resistance $R_{\mathrm{MSM}}(t)$ is related to the time-varying carrier density and is a function of the electrode spacing d such that

$$R_{\mathrm{MSM}}(t) = \frac{d}{Se\mu_e N(t)} \tag{B2}$$

where $\dot{N}(t)$ is obtained from (4) with the condition that, following excitation, the carrier density approaches its quiescent value of $<10^{14}$ cm^{-3}. The rate equation for the charge on an MSM electrode can therefore be written in the form

$$\dot{q}(t) = -q(t)\left[\frac{1}{R_{\mathrm{MSM}}(t)} + \frac{1}{R_{\mathrm{load}}}\right]\frac{1}{C} + I(t) \tag{B3}$$

with the steady-state condition

$$q(t) = q(t + T). \tag{B4}$$

In general, the average charge $\langle q \rangle$ on the MSM capacitor is obtained by numerically solving (B2)–(B4), giving an average voltage signal

$$V = \frac{\langle q \rangle}{C} = \frac{1}{TC}\int_0^T q(t)\,dt. \tag{B5}$$

If $\tau_\omega < \tau_r$, and diffusion effects are negligible (as is the case for LT–GaAs, where the diffusion length for a 1 ps lifetime is 0.06 μm $\ll \alpha^{-1} = 0.7$ μm) one can assume that the carrier density decays exponentially with time constant τ_r. The square-pulse approximation can then also be used to calculate the amount of charge q_o deposited on the electrodes by each current burst

$$q_o = \dot{J}^I S\tau_e^2\left(\frac{\tau_\omega}{\tau_c} + e^{-\tau_\omega/\tau_e} - 1\right). \tag{B6}$$

This derivation ignores Schottky barrier effects and a space-charge field [17] in the vicinity of the electrodes which can inhibit carrier flow onto the electrode. The space-charge field can also vary with time as the electrodes charge. For QUIC current generation by the OPO the steady-state voltages across the MSM gap are sufficiently small that carrier flow is not likely altered during MSM charging. However, in the OPA case, time-dependent space-charge effects may significantly reduce charge collection, explaining the apparently larger discrepancy between theory and experiment.

REFERENCES

[1] E. A. Manykin and A. M. Afanas'ev, "On the possibility of making a medium transparent by multiquantum resonance," *Sov. Phys. JETP*, vol. 25, pp. 828–830, 1967; *J. Exptl. Theor. Phys.*, (USSR), vol. 52, pp. 1246–1249, 1967.
[2] D. J. Jackson and J. J. Wynne, "Interference effects between different optical harmonics," *Phys. Rev. Lett.*, vol. 49, pp. 543–546, 1972.
[3] C. Chen, Y.-Y. Yin, and D. S. Elliott, "Interference between optical transitions," *Phys. Rev. Lett.*, vol. 64, pp. 507–510, 1990.

[4] A. Shnitman, I. Sofer, I. Golub, A. Yogev, M. Shapiro, Z. Chen, and P. Brumer, "Experimental observation of laser control: Electronic branching in the photodissociation of Na$_2$," *Phys. Rev. Lett.,* vol. 76, pp. 2886–2889, 1996.

[5] H. G. Muller, P. H. Bucksbaum, D. W. Schumacher, and A. Zavriyev, "Above-threshold ionization with a two-color laser field," *J. Phys. B,* vol. 23, pp. 2761–2764, 1990.

[6] J. D. Corless and C. R. Stroud, Jr., "Optical mixing of rydberg angular momentum," *Phys. Rev. Lett.,* vol. 79, pp. 637–640, 1997.

[7] B. Sheehy, B. Walker, and L. F. DiMauro, "Phase control in the two-color photodissociation of HD$^+$," *Phys. Rev. Lett.,* vol. 74, pp. 4799–4802, 1995.

[8] Y. E. Kapitzky and B. Y. Zel'dovich, "Second order polarizability holograms in few-mode fibers: Phase conjugation and angular selectivity," *Opt. Lett.,* vol. 15, pp. 1236–1238, 1990.

[9] E. M. Dianov, P. G. Kazanski, and D. Y. Stepanov, "Problem of the photoinduced second harmonic genertion in optical fibers," *Sov. J. Quantum Electronics,* vol. 19, pp. 575–576, 1989 (*Kvantovaya Elektron.,* vol. 16, pp. 887–888, 1989).

[10] D. Z. Anderson, V. Mizrahi, and J. E. Sipe, "Model for second-harmonic generation in glass optical fibers based on asymmetric photoelectron emission from defect sites," *Opt. Lett.,* vol. 16, pp. 796–798, 1991.

[11] A. P. Heberle, J. J. Baumberg, and K. Köhler, "Ultrafast coherent control and destruction of excitons in quantum wells," *Phys. Rev. Lett.,* vol. 75, pp. 2598–2601, 1995.

[12] X. Marie, P. Le Jeune, T. Amand, M. Broisseau, J. Barrau, M. Paillard, and R. Panel, "Coherent control of the optical orientation of excitons in quantum wells," *Phys. Rev. Lett.,* vol. 79, pp. 3222–3225, 1997.

[13] P. Brumer and M. Shapiro, "Coherence chemistry: Controlling chemical reactions with lasers," *Accts. Chem. Res.,* vol. 22, pp. 407–413, 1989.

[14] P. Brumer and M. Shapiro, "Laser control of chemical reactions," *Sci. Amer.,* vol. 272, no. 3, p. 34, 1995.

[15] L. Zhu, V. Kleiman, X. Li, S.P. Lu, K. Trentelman, and R. J. Gordon, "Coherent laser control of the product distribution obtained in the photoexcitation of HI," *Science,* vol. 270, pp. 77–80, 1995.

[16] W. S. Warren, H. Rabitz, and M. Dahleh, "Coherent control of quantum dynamics: The dream is alive," *Science,* vol. 259, pp. 1581–1589, 1993.

[17] M. V. Éntin, "Theory of the coherent photogalvanic effect," *Sov. Phys. Semicond.,* vol. 23, pp. 664–666, 1989 (*Fiz. Tekh. Poluprovodn.,* vol. 23, pp. 1066–1069, 1989).

[18] G. Kurizki, M. Shapiro, and P. Brumer, "Phase controlled current in semiconductors," *Phys. Rev. B,* vol. 39, pp. 3435–3437, 1989.

[19] A. Khan, H. M. van Driel, and X.-Q. Zhou, "Control of photocurrent directionality in semiconductor quantum structures by laser coherence," presented at the Can. Assoc. of Physics Congress, Physics in Canada, paper HB6, June, 1993.

[20] H. M. van Driel and A. Haché, "Control of photocurrent directionality via interference of single and two photon absorption in a semiconductor," in *OSA/IEEE Conf. on Nonlinear Optics; Materials, Fundamentals, and Applications,* Waikaloa, HI, July, 1994.

[21] H. M. van Driel, "Coherence control of photocurrent directionality in semiconductors," in *CAM-94 Physics Mtg., AIP Conf. Proc.,* vol. 342, A. Zepeda, Ed., pp. 161–166, 1994.

[22] R. Atanasov, A. Haché, J. L. P. Hughes, H. M. van Driel, and J. E. Sipe, "Coherent control of photocurrent generation in bulk semiconductors," *Phys. Rev. Lett.,* vol. 76, pp. 1703–1706, 1996.

[23] J. Khurgin, "Generation of the terahertz radiation using the $\chi^{(3)}$ in semiconductors," *J. Nonlinear Opt. Phys. Mater.,* vol. 4, pp. 163–169, 1995.

[24] B. Ya. Zel'dovitch and A. N. Chudinov, "Interference of fields with frequency ω and 2ω in the external photoelectric effect," *Pis'ma Zh. Eksp. Teor. Fiz,* vol. 50, p. 405, 1989.

[25] N. Baranova, A. N. Chudinov, and B. Ya Zel'dovich, "Polar asymmetry of photoionization by a field with $\langle E^3 \rangle \neq 0$: Theory and experiment," *Opt. Commun.,* vol. 79, pp. 116–118, 1990.

[26] Y.-Y. Yin, C. Chen, D. S. Elliott, and A. V. Smith, "Asymmetric photoelectron angular distributions from interfering photoionization proceses," *Phys. Rev. Lett.,* vol. 69, pp. 2353–2356, 1992.

[27] E. Dupont, P. B. Corkum, H. C. Liu, M. Buchanan, and Z. R. Wasilewski, "Phase coherent control of photocurrent directionality in semiconductors," *Phys. Rev. Lett.,* vol. 74, pp. 3596–3599, 1995.

[28] A. Haché, Y. Kostoulas, R. Atanasov, J. L. P. Hughes, J. E. Sipe, and H. M. van Driel, "Observation of coherently controlled photocurrents in GaAs," *Phys. Rev. Lett.,* vol. 78, pp. 306–309, 1997.

[29] J. S. Blakemore, "Semiconducting and other properties of GaAs," *J. Appl. Phys.,* vol. 53, pp. R123–R181, 1982.

[30] E. D. Pallik, *Handbook of Optical Constants of Solids.* New York: Academic, 1985, p. 439.

[31] J. Fraser, A. Haché, J. E. Sipe, and H. M. van Driel, "Three color coherent control of currents in semiconductors," unpublished.

[32] B. S. Wherret, "Scaling rules for multiband interband absorption in semiconductors," *J. Opt. Soc. Amer. B,* vol. 1, pp. 67–72, 1984.

[33] A. L. Smirl, T. F. Boggess, B. S. Wherrett, G. P. Perryman, and A. Miller, "Picosecond optically induced anisotropic state filling in semiconductors," *Phys. Rev. Lett.,* vol. 49, pp. 933–936, 1982.

[34] J. L. Oudar, A. Migus, D. Hulin, G. Grillon, J. Etchepare, and A. Antonetti, "Femtosecond orientational relaxation of photoexcited carriers in GaAs," *Phys. Rev. Lett.,* vol. 53, pp. 384–387, 1984.

[35] C. Aversa and J. E. Sipe, "Coherent current control in semiconductors: A susceptibility perspective," *IEEE J. Quantum Electron.,* vol. 32, pp. 1570–1572, 1996.

[36] S. K. Nayak, T. Sahu, and S. P. Moharty, "Third order nonlinear optical susceptibilities of group IV and III–V compound semiconductors," *Physica B,* vol. 191, pp. 334–340, 1993.

[37] J. H. Collet, "Screening and exchange in the theory of the femtosecond kinetics of the electron-hole plasma," *Phys. Rev. B,* vol. 47, pp. 10279–10291, 1993.

[38] A. Leitenstorfer, C. Fürst, A. Laubereau, and W. Kaiser, "Femtosecond carrier dynamics in GaAs far from equilibrium," *Phys. Rev. Lett.,* vol. 76, pp. 1545–1548, 1996.

[39] D. W. Snoke, W. W. Rühle, Y.-C. Lu, and E. Bauser, "Nonthermalized electrons on a picosecond time scale in GaAs," *Phys. Rev. Lett.,* vol. 68, pp. 990–993, 1992.

[40] S. S. Prabhu, S. E. Ralph, M. R. Melloch, and E. S. Harmon, "Carrier dynamics of low-temperature-grown GaAs observed via THZ spectroscopy," *Appl. Phys. Lett.,* vol. 70, pp. 2419–2421, 1997.

[41] E. S. Harmon, M. R. Melloch, J. M. Woodall, D. D. Nolte, N. Otsuka, and C. L. Chang, "Carrier lifetimes versus anneal in low temperature growth GaAs," *Appl. Phys. Lett.,* vol. 63, pp. 2248–2250, 1993.

[42] X.-Q. Zhou, H. M. van Driel, Z. Gogolak, W. W. Rühle, and K. Ploog, "Femtosecond carrier kinetics in low-temperature-grown GaAs," *Appl. Phys. Lett.,* vol. 61, pp. 3020–3022, 1992.

[43] A. E. Siegman, *Lasers.* Mill Valley, CA: University Science, 1986, p. 332.

[44] L. Qian, S. D. Benjamin, and P. W. E. Smith, "Picosecond optical parametric oscillator tuanble around 1.5 μm," *Opt. Commun.,* vol. 127, pp. 73–78, 1996.

[45] Q. Fu, G. Mak, and H. M. van Driel, "High power, 62 fs optical parametric oscillator synchronously pumped by a 76-MHz Ti-Sapphire laser," *Opt. Lett.,* vol. 17, pp. 1006–1008, 1992.

[46] A. N. Chudinov, Y. E. Kapitzky, A. A. Shulginov, and B. Y. Zeldovich, "Interferometric phase measurments of average field cube $E_\omega^2 E_{2\omega}^*$," *Opt. Quantum Electron.,* vol. 23, pp. 1055–1060, 1991.

[47] A. Haché, "Coherent control of photocurrent in bulk semiconductors," Ph.D. dissertation, University of Toronto, Toronto, ON, Canada, unpublished.

A. Haché, photograph and biography not available at the time of publication.

J. E. Sipe, photograph and biography not available at the time of publication.

H. M. van Driel, photograph and biography not available at the time of publication.